

Use of digital holographic microscopy in tomography

Florian Charrière^a, Frédéric Montfort^a, Jonas Kühn^a, Tristan Colomb^a, Anca Marian^a, Etienne Cuche^b, Pierre Marquet^c and Christian Depeursinge^a

^aEcole Polytechnique Fédérale de Lausanne (EPFL), Imaging and Applied Optics Institute, CH-1015 Lausanne, Switzerland, florian.charriere@a3.epfl.ch

^bLyncée Tec SA, PSE-A, CH-1015 Lausanne, Switzerland, www.lynceetec.com

^cCentre de neurosciences psychiatriques, Département de psychiatrie DP-CHUV, Site de Cery, CH-1008 Prilly-Lausanne, Switzerland

ABSTRACT

Digital Holographic Microscopy (DHM) provides three-dimensional (3D) images with a high vertical accuracy in the nanometer range and a diffracted limited transverse resolution. This paper focuses on 3 different tomographic applications based on DHM. First, we show that DHM can be combined with time gating: a series of holograms is acquired at different depths by varying the reference path length, providing after reconstruction images of slices at different depths in the specimen thanks to the short coherence length of the light source. Studies on enucleated porcine eyes will be presented. Secondly, we present a tomography based on the addition of several reconstructed wavefronts measured with DHM at different wavelengths. Each wavefront phase is individually adjusted to be equal in a given plane of interest, resulting in a constructive addition of complex waves in the selected plane and destructive addition in the others. Varying the plane of interest enables the scan of the object in depth. Thirdly, DHM is applied to perform optical diffraction tomography of a pollen grain: transmission phase images are acquired for different orientations of the rotating sample, then the 3D refractive index spatial distribution is computed by inverse radon transform. The presented works will exemplify the versatility of DHM, but above all its capability of providing quantitative tomographic data of biological specimen in a quick, reliable and non-invasive way.

Keywords: digital holography, tomography, 3D imaging, cell imaging

1. INTRODUCTION

Modern medicine and therapy rely on early and precise diagnosis to permit localized and specific treatments. In particular, imaging the various epithelia at the surface of organs inside or outside the body is of particular importance for the early detection of dysfunction and lesions. Three-dimensional (3D) imaging of complex microscopic and sub-microscopic processes in tissues, down to the cellular level, is still a challenging issue. Rapid, sensitive, non-invasive methods with high-resolution capability are thus needed for diagnosis of lesions or tissue dysfunctions. Digital Holographic Microscopy (DHM) offers new opportunities likely to fulfill these requirements. In DHM the hologram is recorded on a Charge Coupled Device (CCD) camera and reconstructed numerically on a PC, giving direct access to the phase and amplitude of the reconstructed wavefront, with a high vertical accuracy in the nanometer range and a diffracted limited transverse resolution [1-3].

2. HOLOGRAM RECONSTRUCTION

The procedure for hologram processing, in particular for phase reconstruction, is described in details in Refs. 1 and 3. For sake of completeness, a short summary is given here. Holograms acquired by the CCD are first submitted to a procedure of apodization [4] and filtered in the Fourier plane in order to remove the zero order and the twin image [5]. Then, the resulting hologram I_H , is multiplied by a digital reference wave R_D that simulate an illumination wave [1,3] and a propagation calculation in the Fresnel approximation is applied to reconstruct a focused image of the specimen in a plane of coordinates $0\xi\eta$, where a digital phase correction $\Phi(m,n)$ is applied to compensate for the wave front curvature induced by the objective lens (see. Refs. 1,3). In summary, the reconstructed wavefront $\Psi(m\Delta\xi, n\Delta\eta)$, is computed according to the following expression:

$$\Psi(m\Delta\xi, n\Delta\eta) = A\Phi(m, n) \exp\left[\frac{i\pi}{\lambda d} (m^2\Delta\xi^2 + n^2\Delta\eta^2)\right] \times \text{FFT} \left\{ \mathbf{R}_D(j, k) I_H(j, k) \exp\left[\frac{i\pi}{\lambda d} (j^2\bar{x}^2 + k^2\bar{y}^2)\right] \right\}_{m, n}, \quad (1)$$

where m and n are integers ($-N/2 \leq m, n < N/2$), FFT is the Fast Fourier Transform operator, $A = \exp(i2\pi d/\lambda)/(i\lambda d)$, $\Delta\xi$ and $\Delta\eta$ are the sampling intervals in the observation plane, \bar{x} and \bar{y} are the pixel size of the CCD. The digital reference wave is computed using the expression of a plane wave

$$\mathbf{R}_D(j, k) = \exp\left[i(k_{Dx} \cdot j\bar{x} + k_{Dy} \cdot k\bar{y})\right], \quad (2)$$

where k_{Dx} , and k_{Dy} are the two components of the wave vector. The digital phase correction is computed according to the expression of a parabolic wave front

$$\Phi(m, n) = \exp\left(-i\pi/(\lambda d_1)m^2\Delta\xi^2 - i\pi/(\lambda d_2)n^2\Delta\eta^2\right), \quad (3)$$

where parameters d_1 and d_2 define the field curvature along respectively 0ξ and 0η digitally adjusted to correct the defocusing aberration due to the objective lens. $\Delta\xi$ and $\Delta\eta$ are the sampling intervals in the observation plane.

2.1 Parameters adjustment

Eq. 1 requires the adjustment of four parameters for proper reconstruction of the phase distribution. k_{Dx} and k_{Dy} compensate for the tilt aberration resulting from the off axis geometry or resulting from a not perfect orientation of the specimen surface which should be accurately oriented perpendicular to the optical axis. d_1 and d_2 corrects the wave front curvature according to a parabolic model, in principle these two parameters have very similar values, but it may occur in the presence of astigmatism that better results can be achieved with slightly different values. As explained Ref. 1, the parameters values are adjusted in order to obtain a constant and homogeneous phase distribution on a flat reference surface located in or close to the specimen. The manual procedure described in Ref. 1 has been implemented here as a semi automated procedure. First, the program extracts two lines – an horizontal line along 0ξ and a vertical line along 0η – whose location is defined by the operator in the reference surface. Then, one-dimensional (1D) phase data extracted along the two lines are unwrapped in order to remove 2π phase jumps, and a curve fitting procedure is applied to evaluate the unwrapped phase data with a 1D polynomial function of the second order. k_{Dx} and d_1 are iteratively adjusted to minimize the deviation between the fitted curve and the ideal horizontal constant profile. The same way, k_{Dy} and d_2 are adjusted until the vertical profile is as close as possible to the ideal vertical constant profile. In general, less than five iterations are necessary to reach optimal parameters values.

3. OPTICAL COHERENCE TOMOGRAPHY WITH DHM

A hologram results from the interferences between an object wave being scattered a sample and a reference wave. Fig. 1 shows the principle of OCT with DHM. The configuration is basically that of a Michelson interferometer. A hologram is formed by the interference of a beam diffracted by a volume object and a reference wave reflected by a moving tilted mirror. When this technique is combined with the use of light with low temporal coherence, it is possible to perform optical tomography of the specimen.

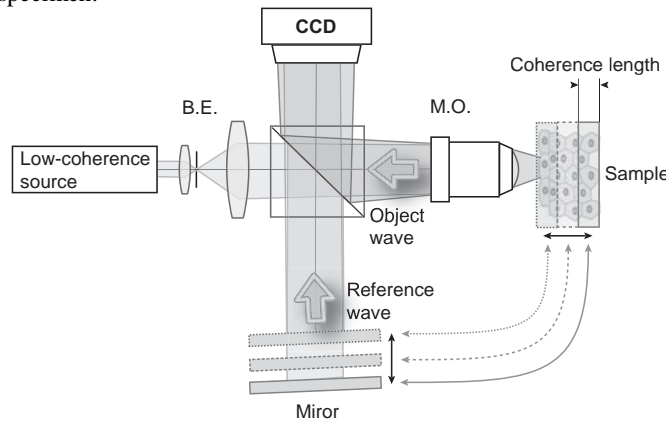


Fig. 1. Schematic of the optical system used to achieve optical coherence tomography with a short coherence digital holographic microscope (B.E. = Beam Expander, M.O. = Microscope Objective).

A series of holograms resulting from the interference of the reference beam and the light diffracted at different depths in the specimen are formed and each of these holograms provide, after wavefront reconstruction, cumulated phase and amplitude data along the optical path, yielding a detailed tomographic image of the object. The thickness of a tomographic layer is half the coherence length of the light source in the medium, due to the reflection setup, what is basically the axial resolution of the system. With a coherence length of $24\ \mu\text{m}$, the axial resolution is though around $12\ \mu\text{m}$ in air. The reconstructed image can be calculated anywhere in the coherence length thanks to the digital focusing capability of DHM. In the present paper, all the images are calculated at the center of the coherence length in the sample where the intensity is maximal, but as in classical microscopy, the reconstructed images contain blurred information from the planes out of the focus plane that are still in the coherence length, but at sensibly lower intensity compared to the in-focus information. The microscope objective (MO) has a magnification of 10x and a numerical aperture of 0.35. The low-coherence source is a linearly polarized Ti:Saphir laser (MIRA) operated at a wavelength of 800 nm and producing 80 fs pulses. A neutral density filter was used for the adjustment of the intensities in the reference arm and the object arm of the interferometer. One or two beam expanders, including pinholes for spatial filtering, are introduced in the arms of the interferometer to produce clean plane waves. The sample is illuminated through the MO with a collimated beam. A variable delay could be introduced between the object wave and the reference wave in order to slide the “coherence gate” and scan the sample in depth. The hologram detection was achieved by a standard 512×512 black and white CCD camera with a lens-on-chip configuration that renders approximately the entire detector area light sensitive. The pixel size was $11\ \mu\text{m} \times 11\ \mu\text{m}$. A frame grabber board installed on the computer was used to perform hologram digitalization. A SNR of 60 dB is achieved by the CCD for the hologram acquisition.

3.1 Application of short coherence DHM to obtain tomographic images of a biological sample: a porcine eye

Several experiments were performed tempting to image the structures in the anterior part of enucleated porcine eyes: 3D tomography of the cornea is presented. Schematic images of the eye and the cornea are shown in Fig. 2a) and 2b). The first layer of the cornea is consisting of a transparent epithelium formed by a layered stack of living cells with a nucleus and cytoplasm. The main structures of the $550\ \mu\text{m}$ thick cornea are the epithelium, the stroma and the endothelium. It should be noticed that Bowman’s membrane (see Fig. 2b) is absent in porcine eyes, used in our experiments. The porcine cornea and epithelium are also thicker than the corresponding human tissues, $700\text{-}800\ \mu\text{m}$ for the cornea and $50\text{-}60\ \mu\text{m}$ for the epithelium, while the endothelium seems to be slightly thinner, about $6\ \mu\text{m}$ [6].

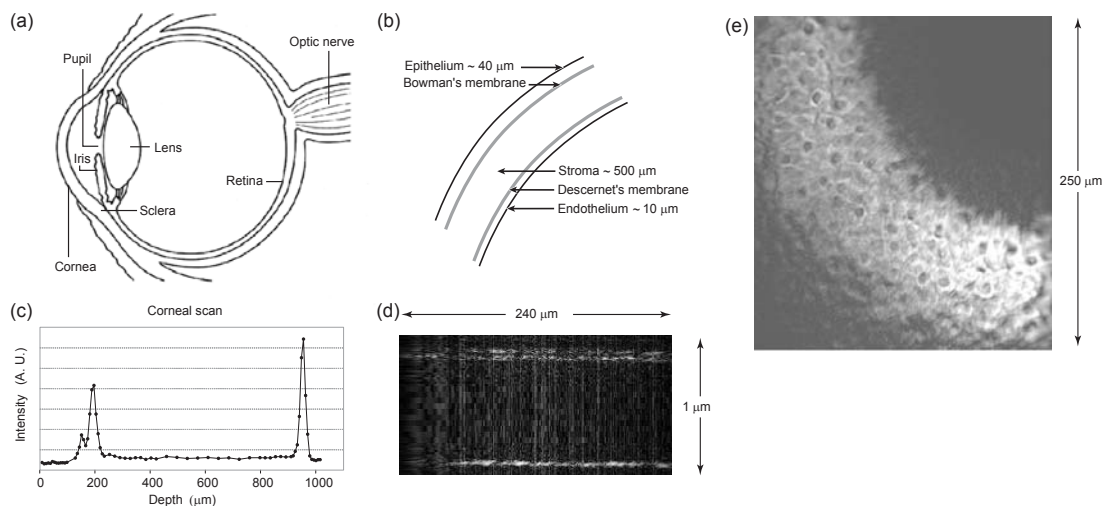


Fig. 2. Schematics of a) the eye and b) the cornea substructure. c) Back scattered intensity when scanning through the cornea. The double peak corresponds to the thick epithelium, while the single peak corresponds the endothelial monocellular layer. d) *Cross-sectional* image of the whole cornea. The two interfaces of the epithelium are visible at the top of the image and the endothelial layer at the bottom. e) *En face image* of porcine corneal epithelium in situ. This tomographic image yields details at the cellular level: image of nuclei and cytoplasm. (The upper-right and lower-left parts of the image contain no information due to the convex form of the cornea).

To be able to penetrate far enough into the eye and extract information from the entire thickness of the cornea, immersion of the eye in a physiological solution (0.9 % NaCl water solution) was performed and the microscope objective placed in the solution. Holograms were recorded every 8 μm in the region of the epithelium and endothelium and every 40 μm in the middle of the stroma. The graph in Fig. 2c) shows the back-scattered signal throughout the whole thickness of the cornea. Each point was obtained by calculating the average intensity over an area of $10 \times 10 \mu\text{m}^2$ in the reconstructed image plane, normal to the scanning direction. The double peak to the left corresponds to the relatively thick epithelium and the peak to the right to the thin monocellular endothelial layer. The thickness of the epithelium was estimated to 50 μm and the thickness of the cornea to around 800 μm .

The cross-sectional image of the section in the cornea is presented in Fig. 2d). The axial resolution of this image is defined by the depth resolution of short coherence DHM (around 11 μm). The pixel size is set to 8 μm , the minimal step length used during recording. The holographic set-up determines the resolution in the plane of the cornea section: around 1 μm for the characteristics of the MO used in these measurements. A pixel size of 1 μm was retained in agreement with the resolution of DHM, and the resolution was proven to be sufficient to observe subcellular details of the epithelial layer inside the 40 μm thick layer (Fig. 2e). The main reflective layers appear slightly tilted relatively to the optical axis (y-axis in the image). This is due to the use of low-coherence light in combination with the off axis geometry of the holographic set-up (beam walk-off), because the fringes on the hologram originate from different depths in the object. The reconstructed image then corresponds to an oblique object slice slightly tilted at an angle in relation to a plane perpendicular to the illumination.

3.2 Discussion on OCT with DHM

It was also demonstrated that imaging different structures in the eye such as the cornea epithelium, could be carried out successfully. It was also shown, for the first time to our knowledge with short coherence digital holographic microscopy, that details could be obtained at the subcellular level on the image of cornea epithelium. The lateral resolution is similar to that obtained by A. Dubois with full field OCT [7], but the axial resolution is worse (11 μm). This is due to the bandwidth of the source, which is only 15 nm in our short coherence DHM setup, what must be compared to the several hundreds of nm for a white light source. This figure could be also improved much in holography by using sources with a broader bandwidth, but a minimal bandwidth must be fixed to preserve the formation of the hologram, i.e. because of the off axis configuration, the coherence length must be sufficient to allow interferences fringes formation over all the chip of the camera. This is the main drawback on axial resolution. The resolution of short coherence DHM is however better than the resolution of ultrasound (35 μm axial) [8] and complementary information might be obtained. Many works remain to improve the significance of the detected signal. In particular the phase information, which results from the numerical reconstruction in digital holography, is not used in the present study. Its potential interest is however great and should be taken into account in the evaluation of the role of the refractive index of tissues along the optical path length.

4. MULTIPLE WAVELENGTHS DHM FOR TOMOGRAPHY

DHM uses of a single hologram taken at a single wavelength and with a single propagation direction of the illuminating wave (single k -vector). Thus, the image also contains information coming from the upper and lower sections of the object, which blur the image and makes this method more suitable for thin objects. Furthermore, the topology of the object is given by the phase information and so it suffers from the phase wrapping problems, which means that the object has to induce a phase shift smaller than the wavelength. It is often not the case and thus an algorithm is needed to unwrap the collected phase. Although these techniques are efficient for relatively smooth objects, their results are in most cases wrong when abrupt edges higher than the wavelength are encountered making the use of DHM with relatively thick objects difficult.

The proposed method uses variable wavelengths illumination waves. The reciprocal space is then scanned by changing the diameter of the Ewald sphere. This technique is developed along the guidelines fixed by the diffraction tomography theorem (see also the pioneering works Refs. 9-12). Digital holography yields a particularly simple way to express "indirectly" the diffraction tomography theorem: remaining in the direct space, tomography of the object can be achieved by the superposition of reconstructed wavefronts from holograms taken at multiple wavelengths. A similar approach has already been proposed several years ago by Marron [13], who has called this method "holographic laser radar". Reference to a similar approach has also been described by Arons and Al. as "Fourier synthesis holography" [14]. More recently, the feasibility of section imaging by wavelength scanning digital holography has been also demonstrated by Kim [15] at a macro-scale. Nevertheless, none of these techniques works at the micro-scale. The introduction of a

microscope objective in the set-up, the use of the retrieved phase for high axial precision measures and a wide wavelength range opens the field of tomography to the sub-microscopic world. Among possible applications are material and life science.

2.2. Multiple wavefronts addition principle

To introduce the multi-wavelength approach, let us state that the diffracted fields of a single hologram Ψ_j , reconstructed in the object plane, creates an exact replica of the object wave Ψ_0 at the object. Let us also consider an object point P located at (x_0, y_0, z_0) which emits a Huyghens spherical wavelet proportional to $A(P)\exp(ikr_{PQ})$ measured at an arbitrary point $Q=(x, y, z)$, where $r_{PQ} = n/r_P - r_Q/$ is the optical pathlength between P and Q , and n is the refractive index. We neglect the $1/r$ dependence of the amplitude. The wave propagates along the z -direction. The factor $A(P)$ represents the field amplitude and phase at the object point. For an extended object, the field at Q is proportional to the above wavelet field integrated over all the points of the object:

$$\psi_j(Q) \propto \sum_{j=0}^{N-1} \psi_j(Q) \propto \iiint A(P) \exp(ikr_{PQ}) d^3r_{PQ} \quad (4)$$

The factor $\exp(ikr_{PQ})$ represents the propagation and diffraction of the object wave. Now assuming that a number N of copies of the electric field distribution are generated by varying the wavelength (and thus the wave number k), all the other conditions of object and illumination remaining the same, let's take N k -vectors k_j regularly separated by dk between k_{\min} and k_{\max} . We have: $k_{\min} = 2\pi/\lambda_{\max}$, $k_{\max} = 2\pi/\lambda_{\min}$, $dk = (k_{\max} - k_{\min})/(N-1)$.

The result of the superposition of these electric fields at Q is:

$$\psi(Q) = \sum_{j=0}^{N-1} \psi_j(Q) \propto \iiint A(P) \exp(i\bar{k}r_{PQ}) T(r_{PQ}) d^3r_{PQ} \quad (5)$$

where $\bar{k} = (k_{\min} + k_{\max})/2$.

$T(r_{PQ})$ can be seen as an amplitude filter function with these extremas:

$$T(r_{PQ}) = \frac{\sin\left(dkr_{PQ} \frac{N}{2}\right)}{\sin\left(dkr_{PQ} \frac{1}{2}\right)} \quad \text{has:} \quad \begin{array}{l} \text{maximas for } r_{PQ} = n \frac{2\pi}{Ndk}, n = mN \\ \text{minimas for } r_{PQ} = n \frac{2\pi}{Ndk}, n \neq mN \end{array} \quad (6)$$

If we consider an infinite wavelength range, then $T(r_{PQ})$ becomes a Dirac function and the resulting wavefront $\mathcal{H}(Q)$ is non-zero only at P . That is, for a large enough number of wave numbers k , the resultant field is proportional to the field at the object, and non-zero only at object points. In practice, if one uses a finite number N of wavelengths at regular intervals dk then the object image $A(P)$ repeats itself at axial distances $\Lambda = 2\pi/dk$ with axial resolution of $\delta = \Lambda/N$. By using appropriate values of dk and N , Λ can be matched to the axial extent of the object and δ to the desired level of axial resolution.

Practically, several equally k -spaced holograms are simulated or experimentally recorded and each hologram is reconstructed independently and stored in its complex form. The phase of these wavefronts is independent of a phase constant, so a reference area may be selected in a reference plane. All the wavefronts to be summed are phase shifted so that the phases in the reference area are set to the same reference value (zero for example). This plane of reference will be the one in which all the unitary vectors will add constructively thanks to the phase adjustment. The points out of this plane will have various phase differences depending on the wavelength, and the unitary vectors will cancel each other when summed. This reference area is to be selected only once. Any further plane of interest distant of an optical path length ϵ from the plane of reference can be derived without having to select a new reference area: knowing equal phases in the reference area, the phase difference $\Delta\phi$ between the new plane of interest and the reference plane is given by $\Delta\phi = (2\pi/\lambda)/\epsilon$. Thus each wavefront will be phase-shifted consequently and when added, the complex wavefronts will be constructive in the new plane of interest, allowing scanning the whole sample in depth.

5. DHM TOMOGRAPHY BASED ON RADON TRANSFORMATION

DHM provides quantitative measurement of the optical path length (OPL) distribution that enable to describe semi-transparent samples, such as living cells with a diffraction-limited transverse resolution and a sub-wavelength axial

accuracy [2]. However, single images as presented in Ref. 2 do not reveal the three-dimensional (3D) internal distribution of cellular components, but a phase shift resulting from a mean refractive index (RI) accumulated over the cellular thickness. We show here that standard optical diffraction tomography (ODT) techniques can be efficiently applied to reveal internal structures and to measure 3D RI spatial distributions. Pioneer works [9-11] have established the theoretical basis of reconstructing the 3D scattering potential of weakly scattering objects, by recording the waves scattered from the different directions of parallel illumination. The experimental setup used in the present work involves a fixed illumination beam and a rotating sample. The main advantages of DHM for complex diffracted wave retrieval is that only a single hologram is needed for each orientation of the specimen, leading to short acquisition time and low stability requirements for the system. The biological specimen observed is a yew pollen grain ($30\ \mu\text{m}$ diameter), having a 3D-structured nucleus, which makes it an ideal test specimen for the method.

5.1 Experimental setup with rotating specimen

Transmission DHM (Fig. 3) used for the present study is described in details in Ref. 1. Results presented here have been obtained with a 63X 0.85 NA microscope objective (MO). The light source is a laser diode at 635 nm. The camera is a 512×512 pixels, 8 bits, black and white CCD, with square pixels of $6.7\ \mu\text{m}$, and a maximal frame rate up to 25Hz. The field of view is $80\ \mu\text{m} \times 80\ \mu\text{m}$. The transverse resolution (around $1\ \mu\text{m}$) and the transverse scale calibration are determined with a USAF 1951 resolution test target.

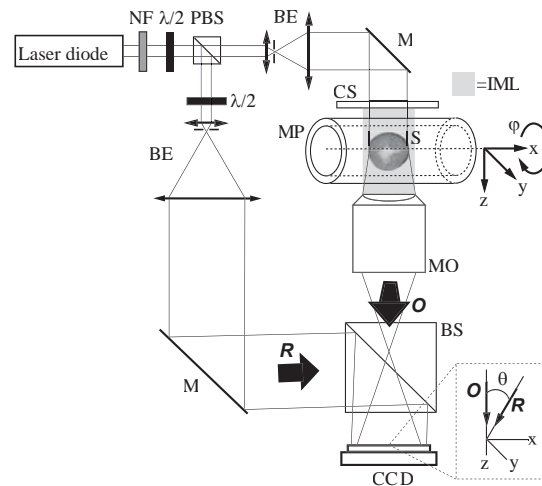


Fig. 3. Digital holographic microscope for transmission imaging: NF neutral density filter; PBS polarizing beam splitter; BE beam expander with spatial filter; $\lambda/2$ half-wave plate; MO microscope objective; M mirror; BS beam splitter; O object wave; R reference wave; MP micropipette; S specimen; IML index matching liquid. Inset: a detail showing the off-axis geometry at the incidence on the CCD.

The pollen cells are in a glass micropipette (MP) filled with a glycerol solution to prevent drying. The MP has an internal diameter of $100\ \mu\text{m}$, an external diameter of $510\ \mu\text{m}$, and is fixed on a micrometric xyz-stage used to center the pollen cell in the field of view. A second xy-stage mounted on the rotating stage itself allows for centering the pollen cell under investigation on the rotation axis, to minimize lateral displacements of the specimen in the field of view during the rotation. The rotation of the stage and the acquisition of the holograms are controlled with a PC. To minimize strong light refraction by the MP, which acts like a cylindrical lens regarding to the illuminating light, the volume between a glass coverslip and the MO is filled with an index matching fluid suppressing the air/glass interface.

5.2 Pollen grain refractive index tomography: results and discussion

In the case of a weakly diffracting object such as a single biological cell, the optical path length of the collimated illuminating photons across the specimen is parallel to the optical axis [16]. The planar phase distribution $\varphi(x,y)$ provided

by DHM is directly proportional to this optical path length. In our experimental setup, the rotation axis is parallel to the x-axis, while the optical axis is the z-axis. $\varphi(x,y)$ can then be expressed as

$$\varphi(x, y) = \int \frac{2\pi}{\lambda} \Delta n(x, y, z) dz,$$

where λ is the wavelength of the light source and $\Delta n(x, y, z)$ is the 3D RI spatial distribution difference between the pollen cell and its surrounding medium. $\varphi(x,y)$ is thus only proportional to the integration of $\Delta n(x, y, z)$ along the z-axis.

To proceed to a standard tomographic reconstruction, one must record such 2-dimensional (2D) planar phase distribution for different sample orientations covering an angle of 180° . In our study, 90 images were acquired with a 2° step at a rate of 1 Hz. The representation of the data as a function of the angle is known as a sinogram.

The 3D signal $\Delta n(x, y, z)$ can be reconstructed from the sinograms by a filtered backprojection algorithm (see for ex. Ref. 17). For this purpose, the standard inverse radon transform *iradon* from the Matlab programming environment was used in a slice-by-slice implementation. The use of filtered backprojection algorithm instead of backpropagation [19] algorithm usually recommended in ODT is consistent with the assumption of a phase proportional to the optical path length across the specimen. The maximal spatial resolution of $\Delta n(x, y, z)$ depends on the sampling step used to cover the 180° during the rotation of the specimen and on the spatial resolution of $\varphi(x,y)$. The 2° step used in this study is sufficient for the maximal spatial resolution to be reached.

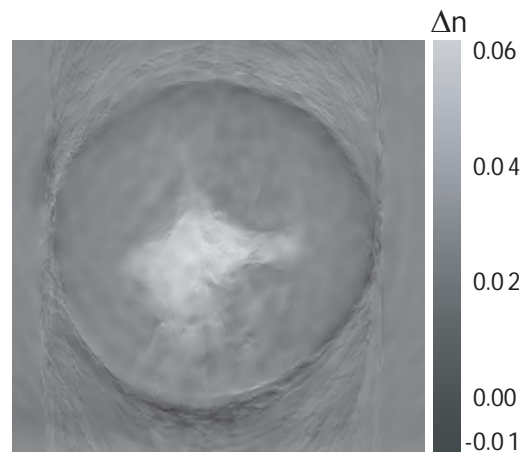


Fig. 4. Tomography of a pollen cell refractive index: cut in the cell along the yz-plane.

The reconstruction is summarized on Fig. 4. Fig. 4 illustrates a cut in the 3D function $\Delta n(x, y, z)$ along the xy-plane in the middle of the pollen cell. On this figure, one can appreciate the 3D structure of the nucleus of the pollen grain. Knowing that the RI of the glycerol surrounding the pollen is 1.473, a $\Delta n=0.06\pm 0.01$ is measured in the nucleus, leading to a measured value of 1.53. The RI of the pollen wall, around $1\ \mu\text{m}$ thick, is not clearly measurable in the present study. As the wall thickness is comparable to the lateral resolution of the system, difficulties appear during the unwrapping procedure involved in the reconstruction process to avoid 2π -jumps in the phase signal, leading to some discrepancies in the phase measurement from an image to another for this critical part of the cell. An increase of the lateral resolution of the system or an adaptation of the embedding medium RI should improve the reliability of the reconstructed phase images. Secondly, the rotation system induces small movements (few microns range). Even if a numerical procedure based on the center of mass determination was used to re-center the cell on its rotation axis, the accuracy of this procedure was also limited to about $1\ \mu\text{m}$, making the tomographic reconstruction of this around $1\ \mu\text{m}$ -thick wall difficult. The slowly varying RI of the $12\ \mu\text{m}$ nucleus is not affected by the two artifacts described above.

The knowledge of the 3D RI spatial distribution of a cell leads to invaluable information concerning the distribution and the optical properties of the intracellular organelles. In spite of this major issue, ODT applied successfully to cell imaging has to our knowledge not provided quantitative results till today [18, 19].

In conclusion, we have shown for the first time to our knowledge the 3D distribution of RI of a semi-transparent object, in our case a pollen grain, provided by backprojecting OPL values collected with DHM on a series of projections of the preparation taken at various incidence angles. The accuracy of the RI determination is better than 0.01 and the 3D spatial

resolution is better than 1 μm in all 3D. This approach could find interesting application as a reference measuring technique in material and life sciences.

CONCLUSION

Through the 3 chosen applications exemplify that DHM is sufficiently robust and versatile, in comparison to other interferometric techniques, to be applied successfully to tomography. More details about the presented works can be found in Refs. 20-22.

ACKNOWLEDGEMENTS

This research has been supported by the Swiss National Science Foundation (SNSF) grant 205320-103885/1. Florian Charrière's email is florian.charriere@a3.epfl.ch.

REFERENCES

1. E. CuChe, P. Marquet and C. Depeursinge, "Simultaneous amplitude and quantitative phase-contrast microscopy by numerical reconstruction of Fresnel off-axis holograms," *Appl. Opt.*, 38, 6994-7001 (1999).
2. P. Marquet, B. Rappaz, P. J. Magistretti, E. CuChe, Y. Emery, T. Colomb and C. Depeursinge, "Digital holographic microscopy: a noninvasive contrast imaging technique allowing quantitative visualization of living cells with subwavelength axial accuracy", *Opt. Lett.*, 30, 468-470 (2005).
3. E. CuChe, F. Bevilacqua, and C. Depeursinge, "Digital holography for quantitative phase contrast imaging", *Opt. Lett.* 24 (5), pp. 291-293 (1999)
4. E. CuChe, P. Marquet and C. Depeursinge, "Aperture apodization using cubic spline interpolation: application in digital holographic microscopy," *Optics Communications* **182**, 59-69, (2000).
5. E. CuChe, P. Marquet and C. Depeursinge, "Spatial filtering for zero-order and twin-image elimination in digital off-axis holography," *Applied Optics* **39**, 4070-4075, (2000).
6. O. Camber, C. Rehbinder, T. Nikkila and P. Edman, "Morphology of the pig cornea in normal conditions and after incubation in a perfusion apparatus", *Acta vet. scand.* **28**, 127-134, (1987).
7. A. Dubois, K. Grieve, G. Moneron, R. Lecaque, L. Vabre, and C. Boccara, "Ultrahigh-resolution full-field optical coherence tomography," *Applied Optics* **43**, 2874-2883, (2004).
8. C.J. Pavlin, F.S. Foster, *High resolution ultrasound*, Ch. 21 in *Cornea*, J.H. Krachmer, M.J. Mannis and E.J. Holland ed., (Mosby, St Louis 1996).
9. E. Wolf, "Three-dimensional structure determination of semi-transparent object from holographic data, " *Opt. Comm.*, 1, 153-156 (1969).
10. W.H. Carter, "Computational reconstruction of scattering objects from holograms", *J. Opt. Soc. Am.* 60, (3), pp. 306-314 (1970)
11. R. Dändliker, K. Weiss, "Reconstruction of three-dimensional refractive index from scattered waves, " *Opt. Comm.*, 1, 323-328 (1970).
12. A.F. Fercher, H. Bartelt, E. Becker, H. Wiltshko, "Image formation by inversion of scattered field data: Experiments and computational simulation", *Appl. Opt.* 18 (14), pp. 2427-2439 (1979)
13. J.C. Marron, K.S. Schroeder, "Holographic laser radar", *Opt. Lett.* 18 (5), pp. 385-387 (1993) 15.
14. E. Arons, D. Dilworth, "Analysis of Fourier synthesis holography for imaging through scattering materials", *Appl. Opt.* 34 (11), pp. 1841-1847 (1995)
15. M.K. Kim, "Tomographic three-dimensional imaging of a biological specimen using wavelength-scanning digital interference holography", *Opt. Express* 7 (9), pp. 305-310 (1999)
16. P. Marquet, "Développement d'une nouvelle technique de microscopie optique tridimensionnelle, la microscopie holographique digitale. Perspective pour l'étude de la plasticité neuronale," MD-PhD Thesis Dissertation (Chapt. 5), UNI-Lausanne, 2003.
17. A. C. Kak and M. Slaney. *Principles of Computerized Tomographic Imaging*. Soc. of Ind. and Appl. Math. SIAM, 2001.
18. V. Lauer, "New approach to optical diffraction tomography yielding a vector equation of diffraction tomography and a novel tomographic microscope," *J. Microsc.*, 205, 165-176 (2002).

19. T. Noda, S. Kawata and S. Minami, "Three-dimensional phase-contrast imaging by a computed-tomography microscope", *Appl. Opt.*, **31**, 670-674 (1992).
20. P. Massatsch, F. Charriere, E. Cuche, P. Marquet, and C.D. Depeursinge, "Time-domain optical coherence tomography with digital holographic microscopy," *Applied Optics*, **44**, 1806-1812 (2005).
21. F. Montfort. "Tomography using multiple wavelengths in digital holographic microscopy" (2005).
22. F. Charrière, A. Marian, F. Montfort, J. Kuehn, T. Colomb, E. Cuche, P. Marquet and C. Depeursinge, "Cell refractive index tomography by digital holographic microscopy," *Opt. Lett.* **31** (2), 178–180 (2006).